Journal of the Meteorological Society of Japan, Vol. 91, No. 4, pp. 431–452, 2013
DOI:10.2151/jmsj.2013-402

Hindcast Prediction and Near-Future Projection of Tropical Cyclone Activity over the Western North Pacific Using CMIP5 Near-Term Experiments with MIROC

Masato MORI, Masahide KIMOTO

Atmosphere and Ocean Research Institute, University of Tokyo, Kashiwa, Japan

Masayoshi ISHII

Meteorological Research Institute, Tsukuba, Japan

Satoru YOKOI, Takashi MOCHIZUKI

Japan Agency for Marine-Earth Science and Technology, Yokohama, Japan

Yoshimitsu CHIKAMOTO

International Pacific Research Center, Honolulu, Hawaii, US

Masahiro WATANABE

Atmosphere and Ocean Research Institute, University of Tokyo, Kashiwa, Japan

Toru NOZAWA

National Institute for Environmental Studies, Tsukuba, Japan

Hiroaki TATEBE

Japan Agency for Marine-Earth Science and Technology, Yokohama, Japan

Takashi T. SAKAMOTO

Atmosphere and Ocean Research Institute, University of Tokyo, Kashiwa, Japan

Yoshiki KOMURO

Japan Agency for Marine-Earth Science and Technology, Yokohama, Japan

Yukiko IMADA

Atmosphere and Ocean Research Institute, University of Tokyo, Kashiwa, Japan

and

Hiroshi KOYAMA

Japan Agency for Marine-Earth Science and Technology, Yokohama, Japan

(Manuscript received 31 July 2012, in final form 18 February 2013)

Abstract

In line with the experimental design for near-term climate prediction toward the Fifth Assessment Report of the Intergovernmental Panel on Climate Change, we perform ensembles of initialized decadal hindcast and near-future projection using three versions of the coupled atmosphere–ocean model MIROC. In the present study, we explore interannual and multiyear predictability of tropical cyclone (TC) activity in the western North Pacific (WNP) using the initialized hindcasts and examine global warming impacts on TC activity in the near-future on the basis of near-future projections up to 2035.

The hindcasts of year-to-year variation in TC number capture the observed values reasonably well. Moreover, interannual variability of TC genesis and occurrence frequency associated with the El Niño Southern Oscillation are found to be predictable, mainly through better prediction of sea surface temperature (SST) and large-scale vorticity anomalies in the lower troposphere. These results indicate that the models can reproduce the major basic mechanisms that link TC genesis with large-scale circulation. Skillful prediction of TC number is likely difficult on multiyear timescales, at least based on our hindcasts, but through initializations, the three-year-mean hindcasts from 1998 onward reasonably capture observed major characteristics of TC activity associated with Pacific climate shift during the late 1990s.

Near-future projections (2016–2035) suggest significant reductions (approximately 14%) in TC number, particularly over the western part of the WNP, even under scenarios in which projected global warming is less prominent than that at the end of this century. This reduction is likely due to the suppression of large-scale lower tropospheric vorticity and relative humidity and the enhancement of vertical wind shear. The projected SST exhibits a more pronounced warming over the eastern tropical Pacific than over the western region and accompanies the weakening of Walker circulation via redistribution of tropical convection activity, which appears to be responsible for the change in the large-scale fields in the WNP.

Keywords near-term prediction; tropical cyclone; global warming

1. Introduction

Near-term (i.e., decadal) climate prediction up to the year 2035 and conventional future projections for the end of the current century will be assessed in the Fifth Assessment Report of the Intergovernmental Panel on Climate Change (IPCC AR5) and the Coupled Model Intercomparison Project Phase 5 (CMIP5) (Taylor et al. 2012). On decadal timescales, in particular, the large-scale climate changes associated with internal variability in the climate system must be considered along with the externally forced component related to global warming (e.g., Collins and Allen 2002; Meehl et al. 2009), because major uncertainties in decadal climate predictions have been found to be more closely related to the predictability of internal climate variations than to global warming (Hawkins and Sutton 2009).

Recently, decadal climate prediction experiments have been performed with initialization; some studies (e.g., Smith et al. 2007, 2010; Keenlyside et al. 2008; Pohlmann et al. 2009; Mochizuki et al. 2010, 2012; Chikamoto et al. 2012, 2013) have successfully predicted regional climate changes on decadal timescales. Smith et al. (2010) demonstrated skillful decadal predictability of the number of tropical cyclones (TCs) in the North Atlantic (NA) basin. Moreover, they highlighted the fact that both internal variability and external forcing are responsible for the recent increase in TC numbers in the NA and demonstrated that model initialization improves prediction skill, mainly through better predictions of tropical Pacific and North Atlantic Ocean conditions. In the western North Pacific (WNP), Chikamoto et al. (2012, hereafter CH12) demonstrated the predictive skills of upper ocean temperature on decadal timescales using initialized hindcasts and demonstrated that the rapid increase in sea surface temperature (SST) anomalies during the late 1990s was predictable. These results give us a hope for better decadal or multiyear predictions of TC activity in the WNP. However, the possibility of skillful decadal or multiyear prediction has not been examined yet.

On the other hand, the possible influence of global warming on TC activity (including genesis number, genesis location, and intensity) has been the subject of considerable research in recent years because of its social (as well as scientific) importance. A number of studies have suggested that TC intensity and global TC

Corresponding author: Masato Mori, Atmosphere and Ocean Research Institute, University of Tokyo, 5-1-5 Kashiwanoha, Kashiwa, Chiba 277-8568, Japan
E-mail: masato@aori.u-tokyo.ac.jp
©2013, Meteorological Society of Japan

number would increase and decrease, respectively, under global warming (e.g., Sugi et al. 2002; McDonald et al. 2005; Oouchi et al. 2006; Gualdi et al. 2008; Zhao et al. 2009; Murakami et al. 2012). However, there seems to be no clear consensus on the impacts of global warming on TC genesis number on a regional basis (e.g., Sugi et al. 2009; Knutson et al. 2010). For the WNP basin, some studies (e.g., Bengtsson et al. 2007; Li et. al. 2010; Murakami et al. 2011) have projected a decreasing trend, whereas others have projected an increasing trend (e.g., Stowasser et al. 2007; Emanuel et al. 2008). Majority of these previous studies assessed changes in TC activity at the end of the present century; consequently, no study to date has addressed near-future (NF) changes in TC activity in the WNP, although Villarini and Vecchi (2012) addressed projected changes in TC genesis frequency in the NA.

In line with the experimental design for near-term climate prediction toward IPCC AR5 and CMIP5, we performed ensembles of initialized decadal hindcasts and NF projection using three versions of the Model for Interdisciplinary Research On Climate (MIROC) (Mochizuki et al. 2010, 2012; Chikamoto et al. 2012, 2013). In the present study, we explore the interannual and multiyear predictability of TC activity in the WNP using these initialized hindcasts. Examination of multiyear predictability in the WNP is more challenging than that in the NA basin, because various large-scale systems (e.g., the Asian summer monsoon) play important roles in TC genesis and location in addition to SST, which is a dominant factor affecting TC activity in the NA (Chia and Ropelewski 2002; Chen and Lin 2011). Here, we also examine the impacts of global warming (i.e., forced response to global warming) on TC activity in the WNP in the NF using the NF ensemble projection of global warming up to the year 2035. Moreover, we adopt a multimodel ensemble approach to determine the aspects of predicted and projected changes that are consistent between models.

The remainder of this paper is organized as follows. Section 2 describes the model, experiments, and analysis methods. In Section 3, we evaluate the predictability of TC activity in the WNP on interannual and multiyear timescales. The results of projected NF changes in TC activity are shown in Section 4, where we also discuss possible mechanisms underlying the projected NF changes paying attention to changes in environmental conditions. Finally, Section 5 presents a summary and discussion of the results.

2. Methods

2.1 Model

The coupled atmosphere–ocean global climate model used is the Model for Interdisciplinary Research on Climate (MIROC), which is a Japanese community model developed collaboratively by the Atmosphere and Ocean Research Institute of The University of Tokyo, National Institute for Environmental Studies, and the Japan Agency for Marine–Earth Science and Technology. A sea ice model and a land model, which includes a river module, are also coupled to the system. No correction is applied for the exchange of heat, water, and momentum fluxes between the atmosphere and the ocean. We use three different versions of MIROC: MIROC3m (Hasumi and Emori 2004; Nozawa et al. 2005), MIROC4h (Sakamoto et al. 2012), and MIROC5 (Watanabe et al. 2010). The resolutions adopted in each model are summarized in Table 1. MIROC3m has been previously used to contribute to the Fourth Assessment Report of IPCC (IPCC AR4) and the Coupled Model Intercomparison Project Phase 3 (CMIP3). The resolution of the atmospheric component is T42 spectral truncation with 20 vertical levels and that of the oceanic component is approximately $1^\circ \times 1^\circ$ (longitude–latitude) grid with 43 vertical levels. MIROC4h adopts the same model physics and dynamical core as the atmospheric component of MIROC3m but is run at a resolution of T213 spectral truncation with 56 vertical levels. The oceanic component has 47 vertical levels and a socalled eddy-permitting horizontal resolution: $1/4^\circ$ in longitude and $1/6^\circ$ in latitude. MIROC5 is a newly developed version, in which most parts of the model physics have been updated or replaced with new parameterization schemes. The resolution of the atmospheric component is T85 spectral truncation with

Table 1. Summary of MIROC versions.

Version	Atm. res.	Ocn. res.	Reference
MIROC3m	T42L20	$1^\circ \times 1^\circ$ grid, L43	Nozawa et al. (2005)
MIROC4h	T213L56	$1/4^\circ \times 1/6^\circ$ grid, L47	Sakamoto et al. (2012)
MIROC5	T85L40	$1^\circ \times 1^\circ$ grid, L49	Watanabe et al. (2010)

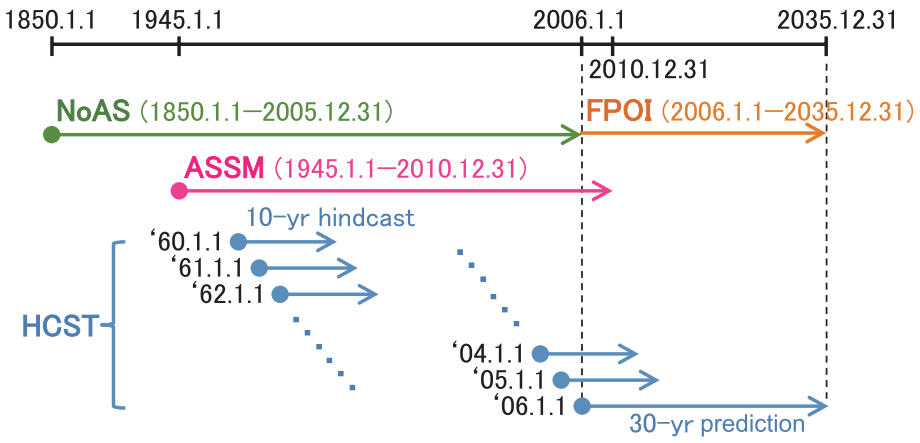


Fig. 1. Schematic of the experimental design for MIROC5. NoAS (green arrow) and FPOI (orange arrow) represent 20th century climate simulation and subsequent future projection, and ASSM (pink arrow) represents the data assimilation experiment. The short and long blue arrows indicate the 10-year hindcast (HCST) and 30-year prediction, respectively.

40 vertical levels and that of the oceanic component is approximately $1^\circ \times 1^\circ$ with 49 vertical levels.

2.2 Experimental design

Before addressing the details of the experimental settings in each model, we first explain the experimental procedure, which is common among the models. A schematic figure of the experimental design for MIROC5 is presented in Fig. 1 as an example. We conduct the following experiments using each of the three versions of MIROC. After a control experiment with fixed external forcing at the preindustrial 1850 level (MIROC3m and MIROC5) or the 1950 level (MIROC4h), we perform the ensemble twentieth century climate simulation (referred to as NoAS), in which the models are integrated with prescribed historical natural and anthropogenic forcing such as greenhouse gases, aerosol concentrations, solar cycle variations, and major volcanic eruptions. These NoAS simulations are started from different initial states obtained from the control simulation. Therefore, each member includes a different phase of internally generated variability, such as the El Niño Southern Oscillation (ENSO) and the Pacific Decadal Oscillation (PDO). The ensemble NoAS simulation is extended up to the year 2035 with future emission scenarios as the subsequent future projection (FPOI). The forcing datasets in NoAS and FPOI are also used as boundary conditions in other experiments. Furthermore, to obtain realistic coupled atmosphere–ocean initial conditions, we perform an ensemble data assimilation (ASSM) experiment by adopting an anomaly assimilation approach (Tatebe et al. 2012). The observed upper ocean temperature and salinity anomalies defined by deviation from the climatology are incorporated into the model anomaly by an incremental analysis update scheme (Bloom et al. 1996). The model climatology is defined by the NoAS experiment. The observed temperature and salinity anomalies, obtained from the gridded monthly objective analysis produced by Ishii et al. (2006) and Ishii and Kimoto (2009), are linearly interpolated to each day and to the ocean model grid. The analysis increment estimated from a spatiotemporally invariant model-to-observation ratio in analysis errors is incorporated into the model as constant forcing in the model tendency equation during an analysis interval of one day. Although all the ensemble members in the ASSM experiment tend to have the same phase of oceanic internal variation influenced by the incorporated observed data, our simple assimilation approach would leave an appropriate amount of difference among the model trajectories in the phase space, particularly in the atmospheric high-frequency states. From the ASSM experiment, we obtain pairs of atmospheric and oceanic initial conditions and conduct a subsequent ensemble hindcast (HCST) experiment. As described below and summarized in Tables 2 and 3, the experimental settings and the number of ensemble members vary among the experiments using MIROC3m, MIROC4h, and MIROC5.

The experimental settings in MIROC3m are almost the same as those in Mochizuki et al. (2010), excluding the hindcast interval. In MIROC3m, each ensemble

Table 2. Summary of experimental settings for the three MIROC versions in the present study.

Version	Exter. forcing	Obs. depth	Obs. data	Init. time of HCST
MIROC3m	CMIP3/A1B	700-m	Ishii et al. (2006)	Every year from 1960
MIROC4h	CMIP5/RCP4.5	3,000-m	Ishii and Kimoto (2009)	Every 5 years from 1991
MIROC5	CMIP5/RCP4.5	3,000-m	Ishii and Kimoto (2009)	Every year from 1960

experiment consists of a 10-member ensemble (Table 3). We perform a 10-member ensemble NoAS simulation for the period 1850–2000 using historical external forcing and an FPOI experiment for the period 2001–2035 with the A1B-type emissions scenario (Nakicenovic et al. 2000). From the 10 members of the NoAS experiment, we obtain 10-member initial states for January 1, 1945 and conduct a 10-member ensemble ASSM experiment for 1945–2010. During data assimilation, temperature and salinity anomalies observed in the upper 700 m of the ocean (Ishii et al. 2006) are incorporated into MIROC3m. On the basis of the 10-member ASSM experiment, we obtain 10-member initial states and conduct 47 sets of 10-year 10-member HCST experiments starting on January 1 each year throughout the period 1960–2006. However, the predictions starting in the year 2006 are extended for 30 years, up to December 31, 2035, under the A1B-type emissions scenario.

In MIROC4h, we conduct a three-member ensemble NoAS experiment for 1950–2005 using the historical forcing dataset for CMIP5 and perform an FPOI experiment for 2006–2035 with the emissions scenario of the Representative Concentration Pathway (RCP4.5; Moss et al. 2008, 2010). However, we use only one member of the NoAS experiment in the present study because the other members do not have the six-hourly outputs necessary for the analysis of TCs. The data assimilation procedure is somewhat different from that of MIROC3m. In terms of horizontal resolution, a small-scale eddy in the ocean is resolved in MIROC4h but not in the observations. When we assimilate the observations with a $1^\circ \times 1^\circ$ horizontal grid into the eddy-resolving MIROC4h, the analysis increment estimated by our system adopted in MIROC3m acts to reduce the small-scale eddy. To retain the small-scale eddy represented in the model, only a large-scale component of the analysis increment estimated from a spatially smoothed field is incorporated into MIROC4h (Tatebe et al. 2012). The observed temperature and salinity anomalies from the surface to 3,000 m depth (Ishii and Kimoto 2009) are assimilated. To reduce computational cost, the ASSM experiment is conducted with one member for the period 1950–2007, and four sets of 10-year four-member ensemble HCST experiments are performed every 5 years starting on January 1 for the period 1991–2006. The predictions starting in 2006 are extended for 30 years to December 31, 2035. Four ensemble members are obtained using the lagged average forecasting (LAF) method (Hoffman and Kalnay 1983) on the basis of a one-member ASSM experiment; for example, for the hindcast starting on January 1, 1991, we define the initial conditions from snapshots of the ASSM results on July 1, 1990, October 1, 1990, December 1, 1990, and January 1, 1991.

Table 3. Number of ensemble members in each experiment. Ensemble members of HCST in MIROC4h and MIROC5 are obtained from the lagged averaged forecast (LAF).

	MIROC3m	MIROC4h	MIROC5
NoAS	10	1	3
ASSM	10	1	3
FPOI	10	3	3
HCST	10	4 (LAF)	6 (LAF)

In MIROC5, we conduct a three-member ensemble NoAS experiment for 1850–2005 and an FPOI experiment for 2006–2035 using the same forcing data as MIROC4h. For the FPOI experiment, we perform additional three sets of three-member ensemble experiments using the RCP2.6, RCP6.0, and RCP8.5 future emission scenarios (Moss et al. 2008, 2010). Similar to the MIROC3m case, we conduct a three-member ensemble ASSM experiment for 1945–2010, in which the observation data used is the same as that in MIROC4h. We conduct 47 sets of 10-year six-member ensemble HCST experiments starting every year on January 1 for the period 1960–2006, and the predictions starting in 2006 are extended for 30 years to December 31, 2035. Because of restricted computational resources, on the basis of only two-member ASSM experiments, we obtain six ensemble members from the LAF method with the previous three- and six-month lags; for example, for the ensemble HCST experiment starting on January 1, 1960, we define the initial conditions using snapshots

Table 4. Threshold values in the TC detection criteria. See list in Section 2.3 for an explanation of these criteria.

	MIROC3m	MIROC4h	MIROC5
P_t (hPa)	0.55	1.0	1.02
ζ_t (10^{-5}s^{-1})	3.0	15.0	1.0
V_t (ms^{-1})	8.0	15.0	8.0
T_t (K)	1.0	1.5	0.8
S_t	1	4	1
D_t	36	42	36

of the ASSM results on July 1, 1959, October 1, 1959, and January 1, 1960.

2.3 Detection algorithm for tropical cyclones

In this study, TCs are detected from six-hourly model outputs on the basis of a set of criteria. Because the resolution of the models is insufficient to simulate realistic TCs, the intensity of simulated TCs is weaker than that of real TCs. However, disturbances with TC-like structures are generated even in MIROC3m, the lowest resolution model. Therefore, the threshold values of criteria for detecting simulated TCs should be more lenient than those for real TCs. Furthermore, because model specifications such as resolution and parameterization schemes are different for each model, it is necessary to optimize different threshold values of the criteria for each model in order to appropriately detect simulated TCs (e.g., Yokoi and Takayabu 2009; Murakami et al. 2012). The thresholds are optimized for each model to ensure that the present-day (PD) annual mean TC number in the WNP basin matches that observed (approximately 27 per year for the period 1979–2007). We adopt the following criteria, and the threshold values are summarized in Table 4.

1) The candidate for TC center is a grid point at which the sea level pressure is lower by at least a chosen threshold (P_t), than the mean over the surrounding 7° × 7° grid box.
2) At the TC center, the magnitude of the relative vorticity at 850 hPa exceeds a chosen threshold (ζ_t).
3) Near the cyclone center, the maximum wind speed at 850 hPa exceeds a chosen threshold (V_t).
4) There is an evident warm core aloft; namely, the sum of the temperature deviations at 250, 500, and 850 hPa exceeds a chosen threshold (T_t). The temperature deviation for each level is computed by subtracting the mean temperature over the surrounding 12° × 12° grid box from the maximum temperature near the center.
5) The maximum wind speed at 850 hPa is greater than that at 250 hPa during the first few time steps (S_t) of the dataset.
6) Criteria 1–4 are satisfied for at least a specified time period (D_t).

These criteria are based on previous studies (Sugi et al. 2002; Murakami et al. 2011) with some modifications. The target area is set as the WNP (defined here as 100–180°E, 0–45°N), but the genesis locations of TCs are limited to the ocean in the region 0–30°N.

A tracking program is developed to search for TCs near the location of the TCs found in the previous time step of the dataset, and the tracks are computed for each TC event. TC positions along the track are counted in each 5° × 5° grid in the WNP at six-hour intervals. The total count for each year and grid box is defined as the TC occurrence frequency (TOF). Similarly, the total count of the TC genesis positions is defined as the TC genesis frequency (TGF). The genesis position is defined as the first position at which all the criteria are satisfied.

2.4 Observational data

The observed TC best-track data provided by the U. S. Navys Joint Typhoon Warning Center for the WNP is used to evaluate the TC prediction in the present-day simulation. We select only TCs with tropical storm intensity or stronger (i.e., TCs that possess 1-min sustained surface wind of 35 knots or greater). The SST data used is from the gridded monthly objective analysis by Ishii and Kimoto (2009), and atmospheric variables are obtained from the reanalysis dataset of the Japanese 25-year Reanalysis Project (JRA-25; Onogi et al. 2007). We also use the National Oceanic and Atmospheric Administration interpolated outgoing longwave radiation (OLR) data for measures of tropical convective activity.

In the present study, for both observations and simulations, annual mean climatologies are defined as the averages during 1979–2007 and the yearly anomalies are defined by deviations from these averages. For the simulations, the climatology of each model is computed from NoAS and ASSM experiments to increase the data sample. Because we use anomaly assimilation techniques, the contribution of assimilated observations to the climatology is small and negligible.

2.5 Climate drift

To distinguish climate signals from unrealistic signals arising from model climate drift during prediction, the drifts are estimated and excluded from

the HCST experiments in each model. The climate drifts A^k_{drf} are estimated as follows:

$$A^k_{drf}(\tau) = \frac{1}{(N-1)M} \sum_{\substack{j=1 \\ j \neq k}}^{N} \sum_{e=1}^{M} A^j_e(\tau), \quad (1)$$

where A is the model-predicted yearly anomaly of interest, such as SST and TGF; $e = 1, \cdots, M$ is the ensemble member; $j = 1, \cdots, N$ is the number of prediction sets initialized from 1960–2006 (1991–2006), that is, $N = 47$ ($N = 4$) in MIROC3m and MIROC5 (MIROC4h); k is a prediction set of interest; and τ is the prediction lead time. In MIROC5, for example, the drift in the prediction starting in the year 2006 is computed from the 46 sets of prediction data for 1960–2005.

As shown in CH12, the HCST experiment in MIROC5 displays an El Niño-like drift pattern. Although we use anomaly assimilation techniques to reduce the model climate drift, an inconsistency in thermocline depth between the observation and model simulation may result in model drift. However, the model drift is small and negligible in both MIROC3m and MIROC4h.

2.6 Multimodel ensemble

To reduce model biases and uncertainty for simulated and predicted TCs in each model, two types of multimodel ensemble approaches are adopted in this study. The first is a simple average, in which the ensemble mean is computed in each model; then, the ensemble means are averaged without weighting. This simple multimodel ensemble is applied when we evaluate the TC count for the entire WNP. The second approach is a weighted average method. In the prediction, it is difficult to detect a significant increase (decrease) in TGF at a grid cell where TGF is overestimated (underestimated) in the PD simulation. As a result, model biases in the PD simulations in terms of TGF spatial distribution are inherited to the hindcast and future change projection (Murakami et al. 2012). Therefore, a weighted model ensemble average is applied, in which we evaluate the horizontal distribution of variables such as TGF and TOF following Murakami et al. (2012):

$$w_i = \frac{T_i}{R_i} \left(\sum_{i=1}^{L} \frac{T_i}{R_i} \right)^{-1}, \quad (2)$$

where w is weighting; $i = 1, \cdots, L$ is the number of models; R is the root mean square error (RMSE); and T is the Taylor skill score (Taylor 2001) of the simulated TGF climatology, calculated with reference to the observed climatology (Table 5). The Taylor skill score, which is a combination of the spatial variance and spatial correlation, ranges from 0.0 (no skill) to 1.0 (perfect skill). With this weighting method, the simulations using MIROC3m, MIROC4h, and MIROC5 contribute 12%, 38%, and 50%, respectively, to the multimodel ensemble mean. In terms of the HCST experiment, MIROC4h has only four prediction sets (starting on January 1 of 1991, 1996, 2001, and 2006); therefore, the simulations using MIROC3m and MIROC5 contribute 20% and 80%, respectively, to the multimodel ensemble mean in the other 43 prediction sets.

Table 5. RMSE and Taylor skill score T (in parentheses) of the simulated climatological mean spatial distribution of TGF as calculated against the observed climatology. Scores are computed for the WNP basin (100–180°E, 0–30°N).

	MIROC3m	MIROC4h	MIROC5
RMSE (T)	0.43 (0.30)	0.28 (0.61)	0.23 (0.66)

The reproducibility of the simulated TGF climatology is better in MIROC4h and MIROC5 than in MIROC3m (Table 5). The main difference in atmospheric model configuration between MIROC4h and MIROC3m is horizontal resolution, whereas that between MIROC5 and MIROC3m is model physics. This suggests that both resolution and physics are important in improving the reproducibility of TGF and TOF.

The simulated TGF and TOF climatology defined by the weighted multimodel ensemble mean is compared with the corresponding observations (Fig. 2). Qualitatively speaking, TGF is reasonably well simulated and exhibits two maxima: one over the South China Sea and the other to the east of the Philippines. However, the multimodel ensemble overestimates the maximum value over the South China Sea and underestimates it east of the Philippines. Accordingly, the observed TOF maximum over the northeast Philippines is underestimated in the simulations (Fig. 2d).

3. Present-day simulation

3.1 Interannual variation in TC number

Now, the predictability of TC activity on an interannual timescale is investigated through HCST experiments; the multiyear predictability is also explored. Figure 3a illustrates the time series of the annual mean TC count anomaly in the WNP for the best-track and ASSM experiments for 1979–2006. The multimodel ensemble mean for the ASSM run captures

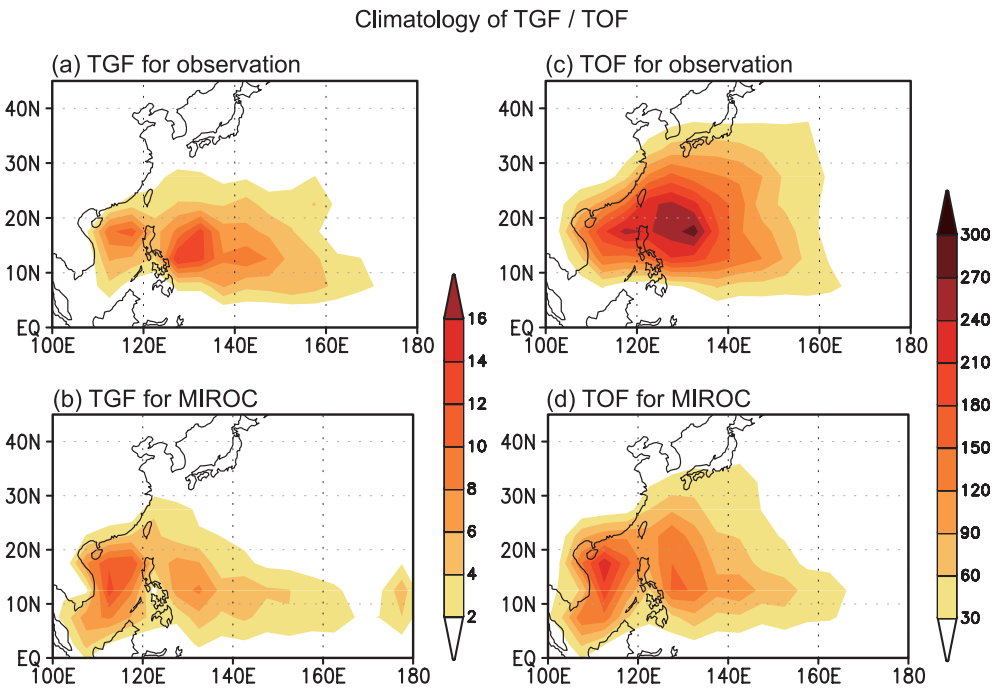


Fig. 2. Annual climatology of (a)–(b) TGF and (c)–(d) TOF during 1979–2007. Observations (top panels) and simulations based on the weighted multimodel ensemble mean (bottom). Units: number per 10 years.

the observed year-to-year variation well, even though only the observed oceanic temperature and salinity are assimilated. The correlation coefficient between these two variables is 0.73 during this period, which is statistically significant at the 99% confidence level (two-sided Student's *t* test). Part of this high correlation can be attributed to the multimodel ensemble approach: the correlation coefficients are 0.59, 0.62, and 0.58 for MIROC3m, MIROC4h, and MIROC5, respectively, and they are also statistically significant at the 99% confidence level. Some recent studies demonstrated that the interannual variation is simulated reasonably well using the high-resolution atmospheric general circulation model (AGCM) when forced by the observed SST (Zhao et al. 2009; Murakami et al. 2011, 2012); our result agrees well with these studies. This high correlation indicates that this system can be used for the prediction of annual mean TC behavior. This is further confirmed by the fact that a series of first-year predictions in HCST experiments capture the observed interannual variation reasonably (Fig. 3b). The correlation coefficient between the best-track and multimodel ensemble mean of the first-year prediction is 0.46, with statistical significance at the 95% confidence level. This relatively low value can be attributed primarily to the less skillful prediction from the late-1980s to the mid-1990s, although prediction has been more skillful during recent years (correlation is 0.74 for 1997–2006). While the correlation coefficient between the NoAS experiments and best-track is 0.20 (Fig. 3c), the relationship is not statistically significant. Therefore, the reasonable prediction in the HCST experiment is the result of initialization.

3.2 Interannual TC variability associated with ENSO

It is well known that the ENSO is the most prominent variability affecting interannual variation of TC activity in the WNP (e.g., Chan 2007; Wang and Chan 2002; Chia and Ropelewski 2002; Camargo et al. 2007), and ENSO has a particular influence on the mean location of TC genesis: TCs tend to form over the southeastern part of the WNP during El Niño years. To examine the predictability of interannual variability in TGF and TOF associated with ENSO, correlation and regression maps between the annual mean observed Nino3.4 index and the TGF/TOF anomaly for ASSM and first-year prediction in HCST are compared with the corresponding observations (Fig. 4). In ASSM, because the TGF fields are noisy, small-

scale structures are somewhat different from those observed (Fig. 4b). However, the large-scale features, in which TC genesis is enhanced over the southeastern part of the WNP basin and suppressed over the northwestern part, correspond well with observations. In the HCST, the observed large-scale features are well predicted in the first-year prediction, although the enhanced region tends to be slightly elongated southward and westward (Fig. 4c).

The observed TOF variation associated with ENSO is characterized by enhancement of frequency over the central and southeastern parts of the WNP basin and suppression over the South China Sea (Fig. 4d); these features are also well simulated and predicted in the ASSM and HCST experiments, respectively (Figs. 4e and 4f). Consistent with the bias in TGF, the TOF predictions also exhibit bias in that the enhanced region tends to be elongated slightly southward and westward (Fig. 4f).

Wang and Chan (2002) highlighted that the lower tropospheric relative vorticity anomalies induced by ENSO act as primary controls of the variation of the mean TC genesis location associated with ENSO over the southeastern part of the WNP. El Niño induces pronounced equatorial westerly wind anomalies and large meridional wind shears, and the low-level vorticity generated acts to help spin up TCs by increasing moisture convergence and entraining potential vorticity into TCs. As a result, the southeastern part of the WNP favors TC generation. Therefore, to make a skillful prediction of TGF variability associated with ENSO, both SST and the low-level vorticity response to ENSO must be well predicted. To check the predictability of ENSO and lower tropospheric vorticity fields, the annual mean anomaly of SST and 850 hPa relative vorticity (denoted as ζ_{850}) for the observation, ASSM, and first-year prediction in HCST are regressed upon the observed Nino3.4 index (Fig. 5). Although the predicted magnitude of SST and ζ_{850} in HCST are somewhat weaker than those in the observations and ASSM, the horizontal structures of both variables are well predicted. SST exhibits an El Niño pattern over the Pacific, and positive ζ_{850} anomalies are induced over the southeastern part of the WNP (Fig. 5c). Thus, we can conclude that the skillful first-year prediction of TC activity associated with ENSO appears to originate in the skillful prediction of SST and the atmospheric low-level large-scale circulation induced by ENSO. These results indicate that the models can reproduce the major basic mechanisms that link TC genesis with large-scale circulation.

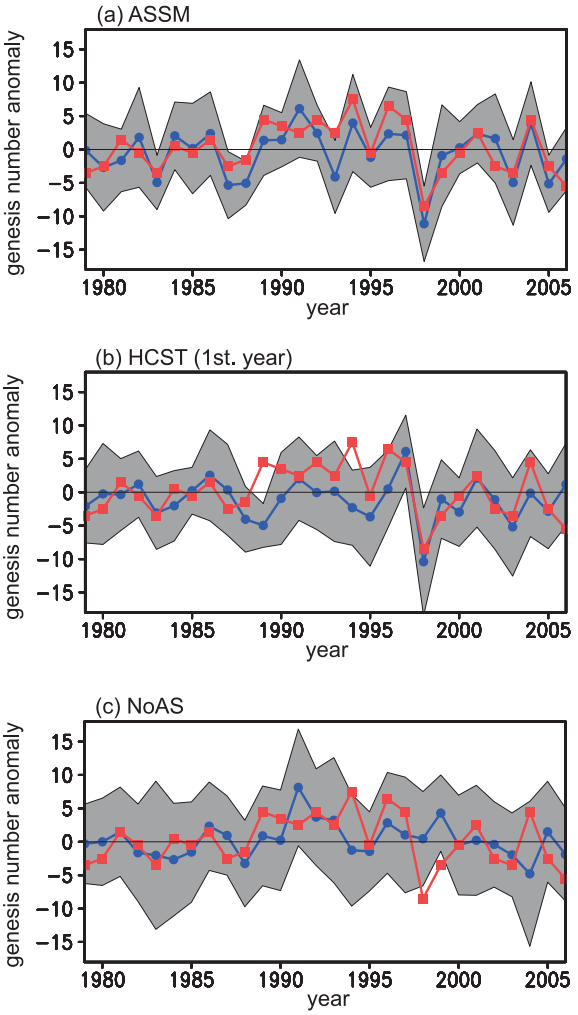


Fig. 3. Yearly variability of annual mean TC count anomaly (unit is yr^{-1}) in the WNP for 1979–2006 based on (a) ASSM, (b) first-year prediction in HCST, and (c) NoAS. The red and blue lines and gray shading represent observation, multimodel ensemble mean, and ensemble spread defined by one standard deviation, respectively.

The predicted positive SST anomaly over the equatorial western Pacific in HCST tends to penetrate further west (around 140°E) than that in the observations and ASSM. This SST bias induces unrealistic positive ζ_{850} anomalies that slightly extend the positive response southward and westward to around 130–140°E. The biases in TGF and TOF are likely caused, to a large extent, by this ζ_{850} bias. Therefore, it is suggested that a more accurate prediction of the El Niño pattern over the equatorial western Pacific is required for more skillful prediction

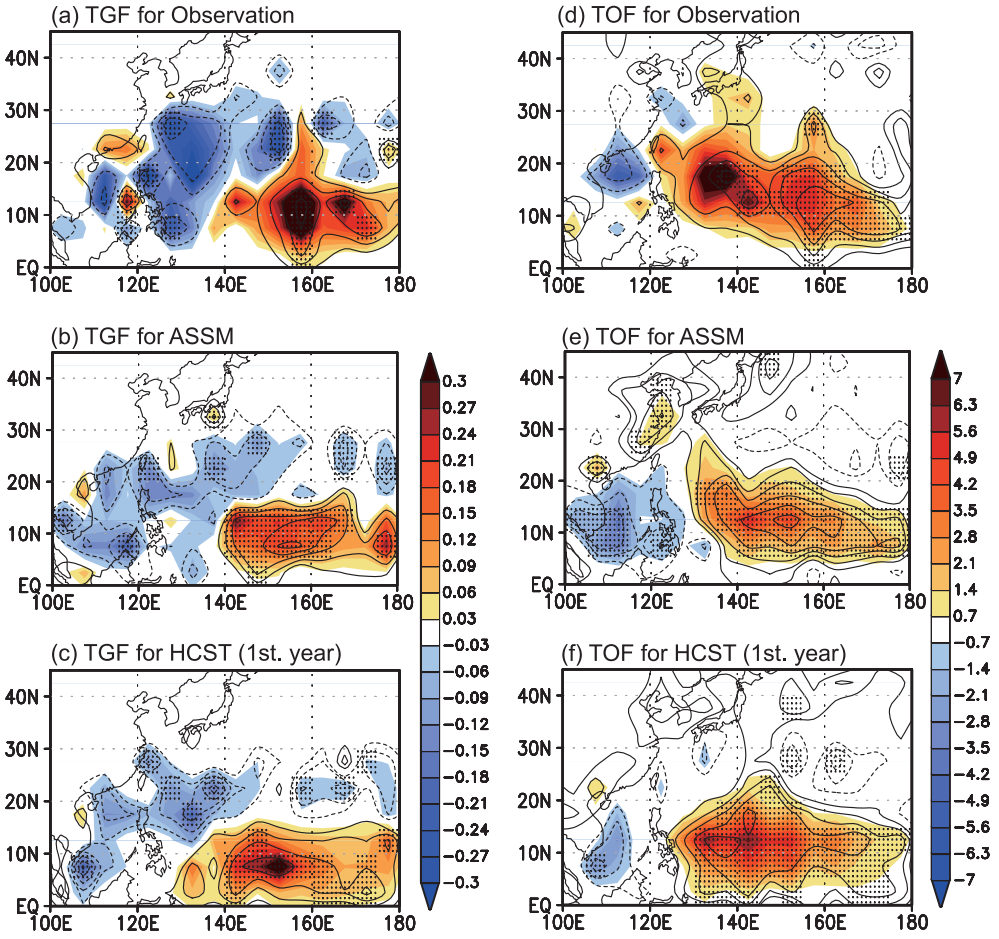


Fig. 4. The annual mean (a)–(c) TGF and (d)–(f) TOF anomalies correlated and regressed upon the observed Nino3.4 index for 1960–2006 based on observations (top panels), ASSM (middle), and first-year prediction in HCST (bottom). The weighted multimodel ensemble mean is adopted in the simulation. The correlation and regression coefficients are represented by contour and shading (units: $yr^{-1}\,K^{-1}$), respectively. Anomalies significant at the 95% confidence level or higher are stippled (two-sided Student's *t* test). The contour interval is 0.1, negative contours are dashed, and the zero contours are omitted.

of TGF and TOF variability associated with ENSO.

It should be noted that the model ensemble mean of the HCST experiment is composed primarily of MIROC3m and MIROC5 because MIROC4h has only four prediction sets starting from the years 1991, 1996, 2001, and 2006. Therefore, these results imply that the model can skillfully predict TGF and TOF variation associated with ENSO regardless of model resolution if SST and atmospheric large-scale fields associated with ENSO are well predicted in the model. This is confirmed by the good result obtained when the prediction sets from MIROC4h are discarded (figure not shown).

To evaluate the time span over which the TGF associated with ENSO remains predictable, the pattern correlation of the regression map between the observations and predictions is calculated in the WNP as a function of prediction lead time (Fig. 6). The correlation coefficient of first-year prediction is 0.52, with statistical significance at the 95% confidence level; this is clearly higher than the NoAS experiment coefficient of 0.08 (two-sided Student's *t* test[1]). Therefore, the reasonable skill in first-year prediction

[1]Based on empirical orthogonal function (EOF) analysis of the observed TGF anomaly in the WNP, 16 EOF modes cover 80% of the total variance of TGF; we use this as the degrees of freedom in the Student's *t* test.

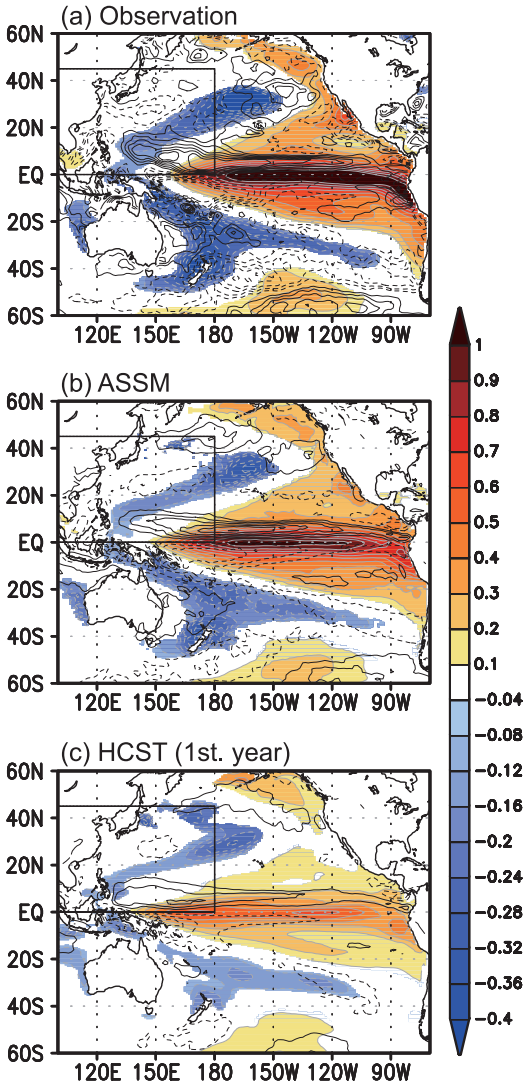


Fig. 5. Same as Fig. 4 but for the regression of SST (shading: units are K K^{-1}) and ζ_{850} (contour: units are 1×10^{-6} s^{-1} K^{-1}) anomalies. (a) Observations, (b) ASSM, and (c) first-year prediction in HCST. Anomalies significant at the 95% confidence level or higher are shaded (two-sided Student's t test). The contour interval is 0.5, negative contours are dashed, and the zero contours are omitted. The observed ζ_{850} is used for the 1979–2006 period.

is found to be the result of initialization. The coefficients of HCST decrease as the lead time increases and are not statistically significant after the second-year prediction. This limitation in predicting more than one year is likely caused by the prediction limit of ENSO (Kirtman et al. 2001).

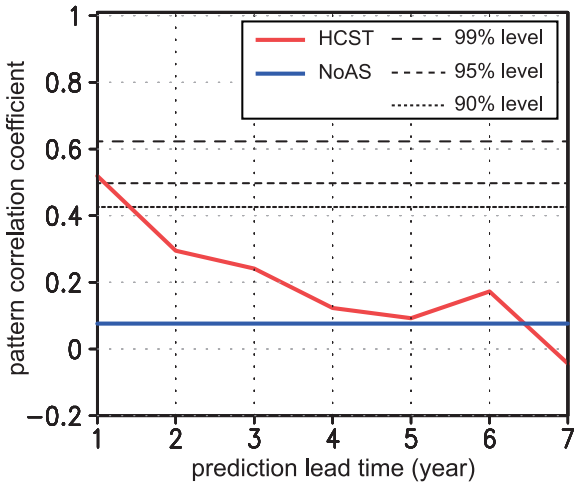


Fig. 6. The pattern correlation coefficients between the regression maps of TGF for the observation and prediction shown in Fig. 4. The red and blue lines represent prediction with (HCST) and without (NoAS) initialization, respectively. Three kinds of black lines represent statistically significant levels (twosided Student's t test). The target area is 100–180°E, 0–30°N.

3.3 *Multiyear predictability of TC activity*

We also explore multiyear predictability of TC activity. Because reasonable predictive skills for upper ocean temperature on decadal timescales have been demonstrated in the WNP basin using initialized hindcasts performed by MIROC models (CH12, the same model used in the present study), it is expected that multiyear TC activity in the WNP will be predictable through reasonable SST prediction. To investigate the possibility of multiyear prediction, time series of TC count anomalies averaged over 1–3 and 1–5 lead years in HCST are compared with the corresponding observations (Fig. 7). For each three- and five-year mean series, the correlation coefficients between the predictions and observations are −0.07 and 0.09, respectively, for 1979–2006. These statistically insignificant coefficients indicate the difficulty in predicting TC genesis number a few years ahead, even when SST is predicted skillfully. As stated in the Introduction, unlike the NA basin, not only SST but also the various atmospheric large-scale systems play important roles in TC genesis in the WNP basin (Chia and Ropelewski 2002; Chen and Lin 2011). Furthermore, there is no significant trend of TC numbers in the WNP, unlike in the NA basin. These factors seem to make multiyear predictions in the WNP more difficult than that in the NA. However, it should be noted that

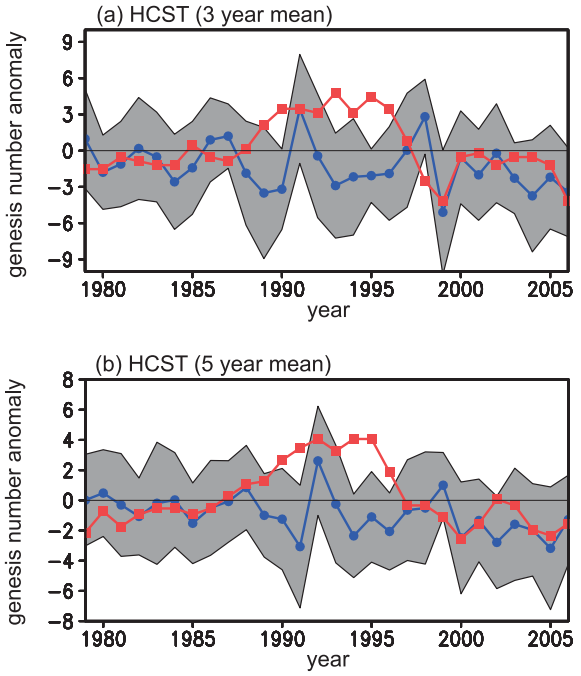


Fig. 7. (a) Three- and (b) five-year mean TC count anomalies (units: yr^{-1}) in the WNP. The red and blue lines represent the observations and multimodel ensemble means for (a) 1–3-year and (b) 1–5-year hindcasts, respectively. The gray shading represents the ensemble spread of prediction defined by one standard deviation. For example, the value at 2000 represents the mean value for 1999–2001 in (a).

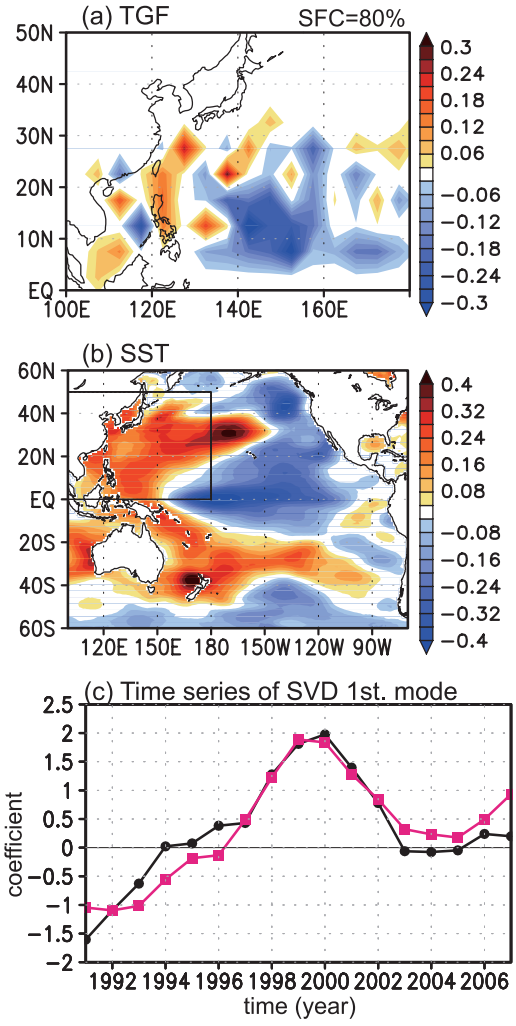


Fig. 8. (a)–(b) Heterogeneous regression maps and (c) time coefficients of the leading SVD mode between the observed three-year mean TGF (units: yr^{-1}) and SST (K) for 1990–2008. The SVD is computed over 100–180°E, 0–30°N. The black and pink lines represent time coefficients for TGF and SST, respectively. For example, the value at 2000 represents the mean value for 1999–2001 in (c). SCF is the squared covariance of a specific SVD mode relative to the sum of all squared covariances between TGF and SST.

when particular years are studied, the predicted number of TCs shows good agreement with the observed number (Fig. 7); for example, both 1–3- and 1–5-year hindcasts started in 1998 predict a prominent negative number anomaly well.

3.4 *Multiyear predictability associated with climate shift*

Recently, CH12 showed that the observed SST anomalies in the western subtropical Pacific of both hemispheres increased rapidly from the early 1990s to the early 2000s, whereas those in the tropical Pacific exhibited a La Niña-like pattern. Moreover, it has been shown that the initialized hindcast can capture the pattern of the SST increase. Thus, CH12 suggested a possible relationship between this climate shift in the Pacific and the abrupt increase in TC occurrence frequency in the vicinity of Taiwan, which was revealed by Tu et al. (2009); however, this relationship has not been examined in detail.

To detect the major spatiotemporal structures of TC activity that are most highly correlated with SST, we perform a singular value decomposition (SVD) analysis between the observed three-year-mean TGF and SST. The heterogeneous regression maps and time series for the leading mode are shown in Fig. 8. The squared covariance fraction (SCF) for the leading

mode is 80% and the correlation coefficient of the two time series is 0.93, indicating a strong connection between TGF and SST. The time series demonstrate that the polarity of this mode changed abruptly during the late 1990s (Fig. 8c), and the SST anomalies associated with this mode exhibit a La Niña-ike pattern that well resembles the climate shift pattern detected in CH12 (Fig. 8b). Furthermore, the pattern of observed TOF variation associated with this mode (Fig. 9) is similar to that presented by Tu et al. (2009), which is characterized by an increase in TOF anomalies around Taiwan and a decrease in other regions. Therefore, this mode can be considered to correspond to the climate shift documented during the late 1990s in CH12. These results indicate that the abrupt changes in TC activity are strongly affected by the oceanic climate shift. As shown in CH12, the SST change associated with the climate shift is predictable in our HCST experiments, which is encouraging for better multiyear prediction of TC activity associated with the climate shift during the late 1990s.

We also investigate the predictability of TC activity associated with this climate shift using three-year-mean HCST experiments. We concentrate on the 1–3-year hindcast starting in 1998, because it exhibits good prediction of the number of TCs (Fig. 7a). Figures 10a–c illustrate the observed TGF, TOF, and SST anomalies averaged over 1998–2000 and the corresponding prediction starting in 1998; in this case, the prediction is based on the multimodel ensemble means of MIROC3m and MIROC5. The observed horseshoe-shaped pattern of SST warming in the WNP is reasonably predicted, but the La Niña-like cooling is overestimated over the western equatorial Pacific around 130–160°E, and the meridional expansion of the cooling is weaker than that observed over the southeastern part of the WNP around 170–180°E (Fig. 10c). The observed TGF exhibits a La Niña-like pattern that is consistent with SST change (Fig. 10a; see also Fig. 4a, in which the polarity is opposite); that is, TC genesis is suppressed and enhanced over the southeastern and northwestern parts of the WNP, respectively. The signal of this large-scale suppression is simulated in the prediction, although the signals lie slightly westward and southward of the observations (Fig. 10a). Furthermore, the prediction underestimates the enhancement of TC genesis over the northwestern part of the WNP. These errors are naturally inherited in the TOF prediction (Fig. 10b). The prediction errors in SST appear to be responsible for those in TGF and TOF, because the SVD analysis indicates a strong relationship between TC activity and SST. It should be noted that similar aspects are obtained even in the 2–3-year hindcast starting in 1998 (Figs. 10d–f), indicating that the hindcasts with more than one year of leading time also capture the observed characteristics reasonably well and contribute to the predictability.

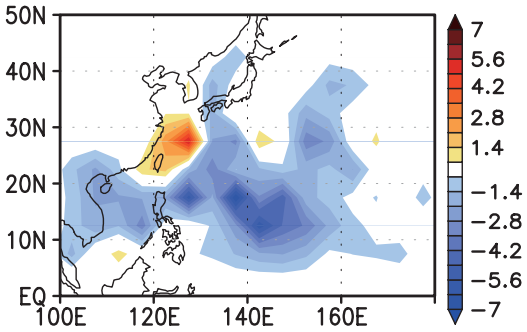


Fig. 9. Three-year mean observed TOF anomalies (units: yr^{-1}) regressed upon the SVD index for SST shown in Fig. 8(c).

Although the observed major characteristics for each variable seem to be predicted reasonably well in our 1–3-year hindcast, the pattern correlation coefficient (0.40) between the predictions and observations of TGF in the WNP is statistically insignificant (TOF and SST are significant at the 90% confidence level, according to the two-sided Student's *t* test), mainly because the negative anomalies are out of position. However, the predicted TGF anomalies obviously occur in response to the predicted La Niña-like SST anomaly. Therefore, we can regard these results as promising, and it is anticipated that the improvement of SST prediction associated with climate shift will allow better prediction of multiyear TC activity associated with the shift.

Although CH12 indicated that rapid SST warming can be explained partly by the forced component related to global warming signals, the pattern correlation coefficient for TGF between the observations and NoAS experiment is 0.03 (figure not shown); this is clearly lower than that in the initialized prediction. This indicates that the pattern of TGF response is sensitive to the shape of the underlying SST, because the SST anomaly in the NoAS experiment does not show La Niña-like cooling over the western equatorial Pacific (figure not shown).

4. Projected near-future change

4.1 TC genesis number

Potential NF changes in TC activity in the WNP have been investigated by future ensemble projection

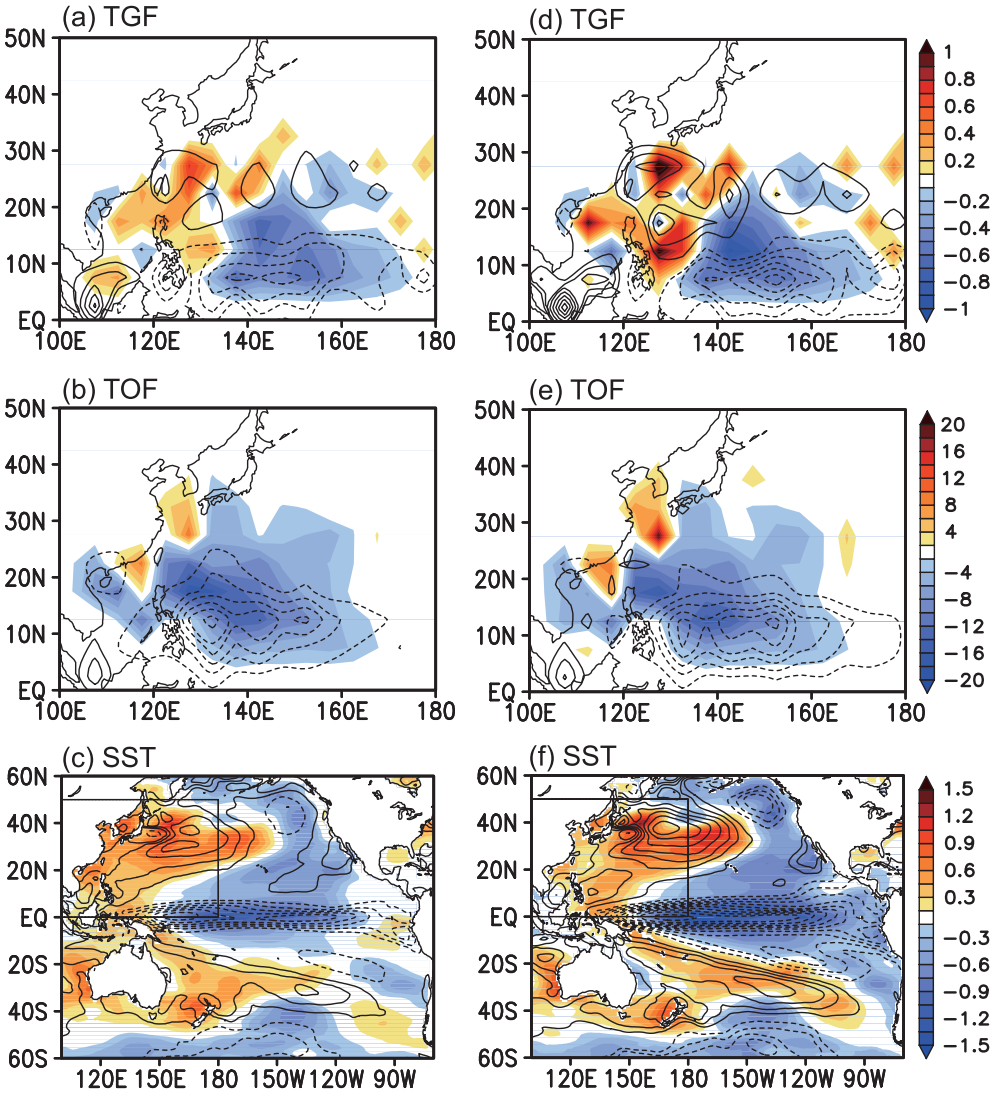


Fig. 10. Three-year mean (for 1998–2000) anomalies of (a) TGF, (b) TOF, and (c) SST for observations (shading) and weighted multimodel ensemble means of 1–3-year hindcast starting in 1998 (contour). (d)–(f) same as (a)–(c), but for two-year mean anomalies (for 1999–2000) of observations (shading) and 2–3-year hindcasts (contour). The contour intervals are (a,d) 0.1 yr^{-1}, (b,e) 2 yr^{-1}, and (c,f) 0.15 K. The negative contours are dashed and the zero contours are omitted.

from 2006 to 2035. Because it is assumed that initialization has no impact on projections 30 years into the future, both uninitialized predictions (FPOI) and initialized predictions for 2006–2035 are used without distinction (36 members are used), and we concentrate on the estimation of NF changes related to global warming (i.e., forced response). Figure 11 illustrates the time series of annual mean TC count anomalies in the WNP for the multimodel ensemble mean of the 30-year future projection, revealing a decreasing trend in TC genesis number; this trend is statistically significant at the 95% confidence level for the period 2006–2035. The projected NF changes in annual mean genesis number are estimated by the difference between the PD simulation (1979–2007) and NF projection (2016–2035) for multimodel ensemble mean and ensemble mean in each model (Fig. 12 and Table 6); the ASSM and NoAS experiments are used as the PD simulation. In all models, the mean genesis number decreases significantly in the NF. The

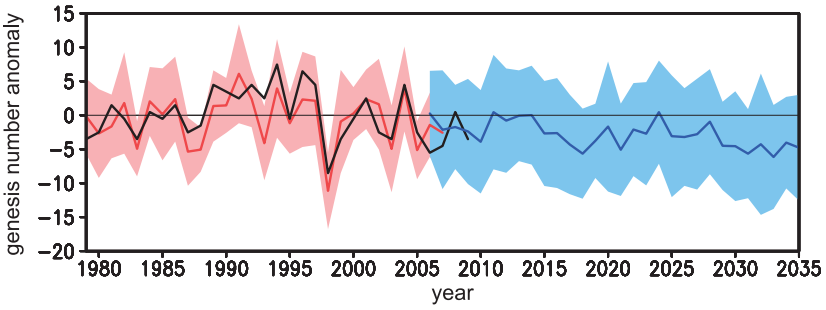


Fig. 11. Yearly variability of annual mean TC count anomaly (units: yr^{-1}) in the WNP based on observations (black line), ASSM (red), and NF projection (blue). The red and blue shading represent the ensemble spreads of ASSM and NF projection, respectively, defined by one standard deviation.

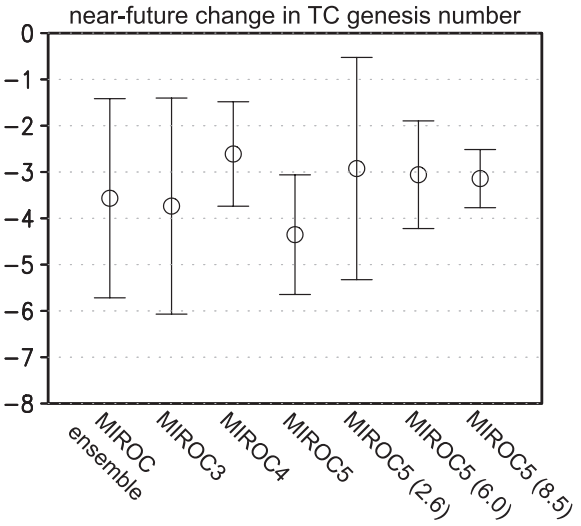


Fig. 12. Difference between the PD simulation (1979–2007) and NF projection (2016–2035) for the total annual number of TCs formed (units: is yr^{-1}) in the entire WNP basin. Circles and bars represent the ensemble mean and ensemble spread defined by one standard deviation, respectively.

ensemble spread of the projection for each model indicates that there are no significant differences in the decreasing number among models. The annual total number of TCs in the multimodel ensemble mean is 22.8 for the NF projection, representing a reduction of 13.6% compared with the PD simulation. Although this reduction is smaller than that estimated by previous studies assessing potential far-future change when the global warming signal is prominent (see Table S1 in the review of Knutson et al. 2010), it is statistically significant at the 99% confidence level. This indicates a possibility that the TC genesis number would decrease significantly even in the near-future when global warming is less prominent than that at the end of this century.

Table 6. Annual mean TC numbers in the WNP for the PD (1979–2007) simulation and NF (2016–2035) projection, projected near-future changes in the annual mean TC number (%), and the level of statistical significance of the change (two-sided Student's *t* test).

Version	PD	NF	NF-PD	SIG
MIROC ensemble	26.4	22.8	−13.6%	99%
MIROC3m	26.2	22.4	−14.5%	99%
MIROC4h	27.0	24.4	−9.6%	95%
MIROC5	25.9	21.6	−16.6%	99%
MIROC5 (RCP2.6)	25.9	23.0	−11.2%	95%
MIROC5 (RCP6.0)	25.9	22.9	−11.6%	95%
MIROC5 (RCP8.5)	25.9	22.8	−12.0%	99%

To estimate the extent to which future emission scenarios could make significant differences in the NF projection in terms of the number of TCs, the NF changes in the annual mean genesis number projected by MIROC5 under RCP2.6, RCP6.0, and RCP8.5 scenarios are compared with those under the RCP4.5 scenario (Fig. 12 and Table. 6). The mean decreases in numbers and ensemble spreads in each projection indicate that the projection uncertainty arising from the scenario is small, at least in the NF, which is consistent with Villarini and Vecchi (2012). However, it should be noted that there are only three ensemble members in the three additional scenario experiments; therefore, internal variability (such as ENSO and PDO) can affect the mean decreases in number and spread. Therefore, the number of ensemble members must be increased to obtain a more reliable estimate of the uncertainty arising from the use of various emissions scenarios.

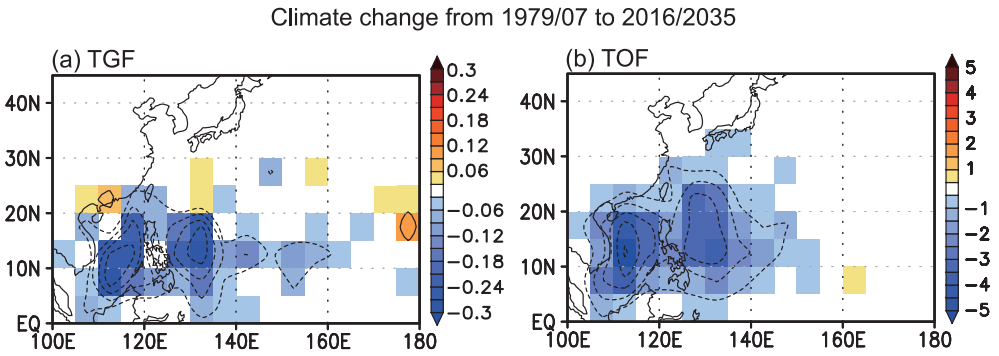


Fig. 13. Projected NF changes (difference between 1979–2007 and 2016–2035 means) in (a) TGF (contour interval: 0.06 yr^{-1}) and (b) TOF (1.0 yr^{-1}) based on the weighted multimodel ensemble mean. Anomalies significant at the 99% confidence level are shaded (two-sided Student's *t* test). The negative contours are dashed and the zero contours are omitted.

4.2 TC genesis and occurrence frequency

Figure 13 illustrates the projected NF change from a PD simulation for weighted multimodel ensemble means of TGF and TOF, demonstrating significant reduction in TC genesis and occurrence frequency over the western part of the WNP. This projected feature is qualitatively very similar to recent results reported by Murakami et al. (2012), who performed a multimodel future projection for the end of this century (2075–2099) using two versions of MRI-AGCM with resolutions of 20 km and 60 km. Quantitatively, the reductions in TGF and TOF are naturally smaller than those for the projection of Murakami et al. (2012). The mechanisms responsible for these NF changes in TGF are discussed below.

4.3 Mechanisms of near-future changes in TC genesis

To discuss reasons for the projected reduction of TC genesis in the WNP, we examine global warming impacts on the large-scale environmental conditions that are considered to influence TC genesis. Those favorable for TC genesis include high SST, lower tropospheric cyclonic circulation, weak vertical wind shear, high relative humidity in the lower and middle troposphere, and low atmospheric static stability (Gray 1975). Maximum potential intensity (MPI), which represents the upper limit of maximum cyclonic wind speed of TCs, has been defined by Bister and Emanuel (1998, 2002) as the combined effects of SST and static stability. Higher MPI means more favorable conditions for TC genesis (Emanuel and Nolan 2004). We investigate the NF changes in ζ_{850}; vertical wind shear, defined as the absolute value of the vector wind difference at 850 and 200 hPa ($V_{shear} = \sqrt{(u_{850}-u_{200})^2+(v_{850}-v_{200})^2}$); relative humidity at 700 hPa (Rh_{700}); and MPI. Figure 14 illustrates the PD simulation (left panels) and projected NF changes (right panels) for each factor according to the weighted ensemble mean during July–November. In the PD climate simulation, TCs are generated more frequently over the area where ζ_{850}, Rh_{700}, and MPI are high and V_{shear} is low (Figs. 14a–d and Fig. 2b).

The projected NF changes in ζ_{850} indicate significant reduction of the monsoon trough over the western part of the WNP (Fig. 14e), which would act to suppress TC genesis there. The enhancement of V_{shear} over the central WNP would also lead to a decrease in TC genesis, although the negative anomalies over the southwestern part of the WNP act in the opposite sense (Fig. 14f). Rh_{700} shows significant reduction throughout the WNP basin, which is also unfavorable for TC genesis (Fig. 14g). In contrast, the change in MPI is favorable for TC genesis, showing significant enhancement over the South China Sea and the northern part of the WNP (Fig. 14h). Although it is difficult to quantitatively estimate the extent to which environmental factors could decrease TC genesis number, a comparison between Fig. 13a and Figs. 14e–h indicates that the projected changes in ζ_{850}, V_{shear}, and Rh_{700} are likely responsible for the NF reduction in TC genesis.

The cause of these changes in the large-scale fields in the WNP may be explained by the weakening of Walker circulation, as described below. The weighted multimodel ensemble mean projects a statistically significant warming of the entire tropical and subtropical upper ocean in the NF (Fig. 15e), although

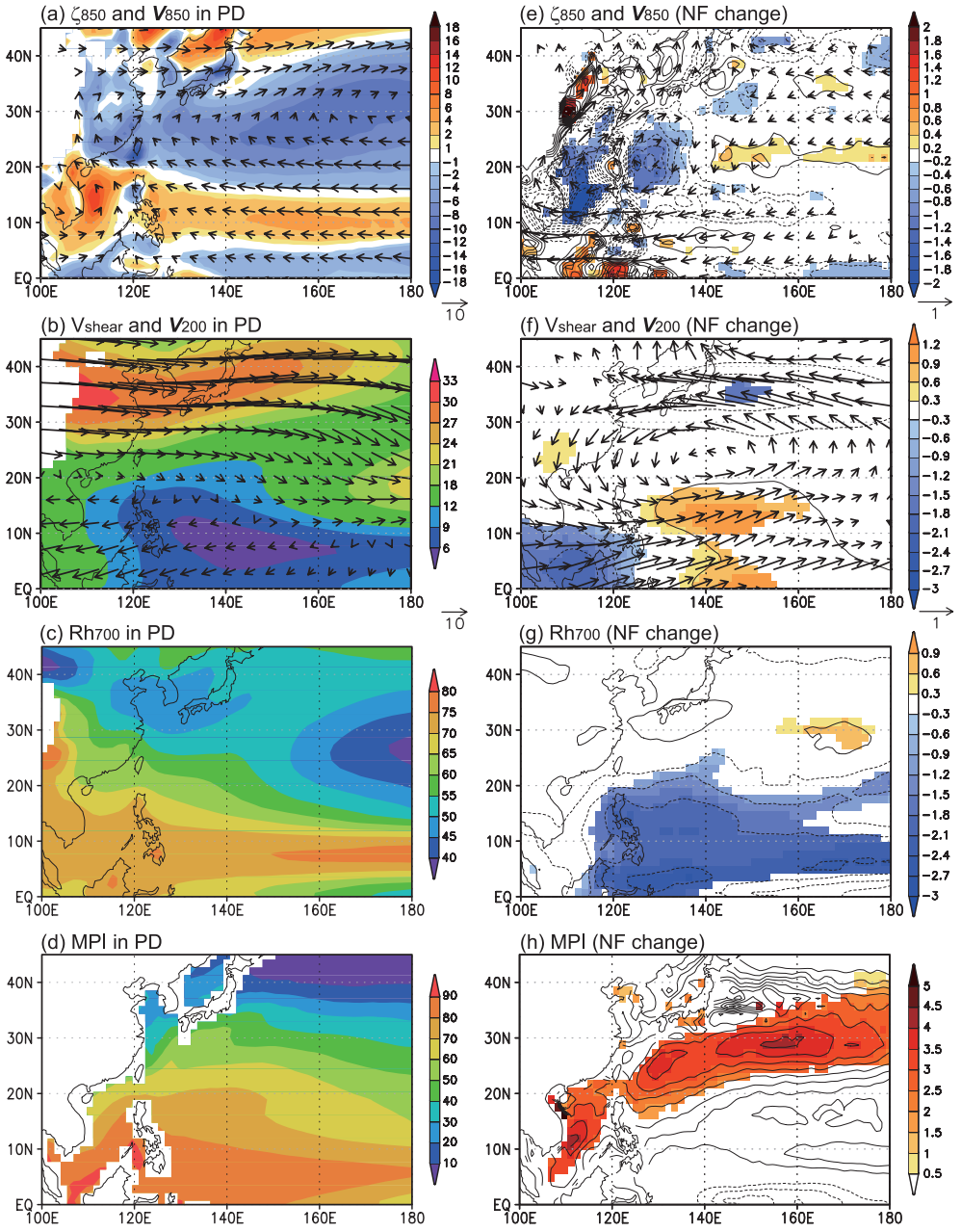


Fig. 14. PD simulation (1979–2007 mean: left panels) and projected NF changes from the PD simulation (difference between 1979–2007 and 2016–2035 means: right) for large-scale seasonal (July–November) environmental conditions according to the weighted multimodel ensemble mean. (a,e) ζ_{850} (unit is 1×10^{-6} s^{-1}) and $\boldsymbol{V}_{850}$ (arrow: m s^{-1}), (b,f) V_{shear} (m s^{-1}) and $\boldsymbol{V}_{200}$ (arrow: m s^{-1}), (c,g) Rh_{700} (%), and (d,h) MPI (m s^{-1}). In the NF change, anomalies significant at the 90% confidence level or higher are shaded (two-sided Student's t test). The contour intervals for each variable are (e) 0.2, (f) 0.6, (g) 0.6, and (h) 0.5. The negative contours are dashed, the zero contours are omitted, and scaling for the arrow is given in the lower right corner.

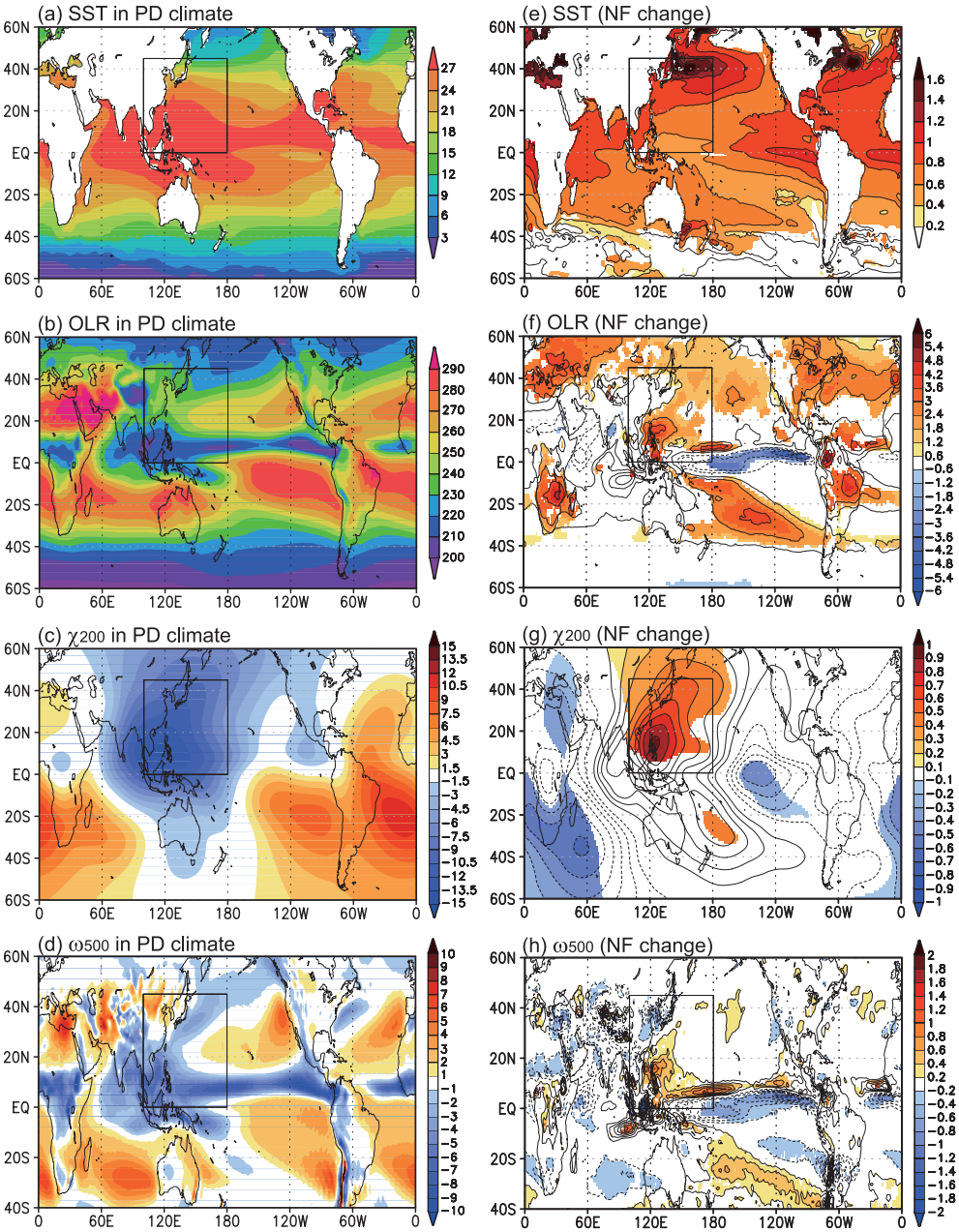


Fig. 15. Same as Fig. 14 but for (a,e) SST (units: K), (b,f) OLR (W m^{-2}), (c,g) χ_{200} (1×10^6 m^2 s^{-1}), and (d,h) ω_{500} (1×10^{-4} hPa s^{-1}). The contour intervals for each variable are (e) 0.2, (f) 1.2, (g) 0.1, and (h) 0.2.

the magnitude of this warming is clearly weaker than that in the multimodel climate projection of CMIP3 models for the end of this century (e.g., Fig. 2 in Murakami et al. 2012). However, the increase in the SST is nonuniform and the eastern tropical Pacific exhibits more pronounced warming. In association with this SST change, projected NF changes in OLR, velocity potential at 200 hPa (χ_{200}), and pressure velocity at 500 hPa (ω_{500}) also exhibit zonally asymmetric changes in the tropical Pacific (Figs. 15f–h), i.e., cumulus convection activities are enhanced over the central and eastern equatorial Pacific but suppressed in the WNP (Fig. 15f). Consistent with this change, upper tropospheric divergence (convergence)

fields in the WNP (eastern tropical Pacific) are significantly suppressed (Fig. 15g), and this suppression is accompanied by middle tropospheric downward (upward) flow anomalies in the WNP (eastern Pacific) (Fig. 15h). These projected changes in global-scale atmospheric circulation, accompanied by the redistribution of tropical convection activity, can be interpreted as the weakening of Walker circulation. This is consistent with findings from the multimodel climate projections of CMIP3 models (Vecchi and Soden 2007) and historical observations from the last six decades (Tokinaga et al. 2012).

Changes in Walker circulation can have considerable impact on environmental conditions in the WNP. NF changes in the upper and lower tropospheric wind fields exhibit cyclonic and anticyclonic circulation anomalies, respectively, in the WNP (Figs. 14e and 14f). These can be interpreted as a Rossby wave response to cooling anomalies associated with the suppression of convective activity in the WNP (Fig. 15f). The atmosphere baroclinic response acts to increase the V_{shear} anomalies by reinforcing lower tropospheric easterly and upper tropospheric westerly wind over the central WNP (around 140°E, 15°N) (Fig. 14f). Therefore, the projected reduction of ζ_{850} over the western part of the WNP and the enhancement of V_{shear} over the central WNP are likely due to the weakening of Walker circulation. The projected decrease in Rh_{700} is accompanied by the descending motion anomaly associated with the weakening of Walker circulation (Fig. 15h). Thus, we conclude that the projected reduction of TC genesis in the WNP is likely due to unfavorable changes in local environmental fields associated with the weakening of Walker circulation. The remote influence of projected eastern tropical Pacific SST warming on TC genesis in the WNP via the weakening of Walker circulation has also been suggested in some previous studies assessing changes in TC activity at the end of this century (e.g., Li et al. 2010; Murakami et al. 2011, 2012).

5. Summary and discussion

In line with the experimental design for near-term climate prediction toward IPCC AR5 and CMIP5, we have performed ensembles of initialized decadal hindcast and NF projection using three versions of MIROC, a coupled atmosphere–ocean climate model. In the present study, we explore interannual and multiyear predictability of TC activity in the WNP using the initialized hindcasts. Moreover, we examine global warming impacts (i.e., forced response to global warming) on TC activity in the WNP in the NF using the NF ensemble projection of global warming up to the year 2035. The simulated TC-like disturbances are detected as TCs from six-hourly model outputs. We adopt the multimodel ensemble approach to reduce model biases and the uncertainty of predicted and projected TCs in each model.

On the interannual timescale, our first-year prediction reasonably predicts year-to-year variation in the number of TCs in the WNP basin, and the predictability is more skillful for recent years (i.e., from the late 1990s to 2006). The predictability of interannual variation of TC genesis and occurrence frequency (TGF and TOF) is also examined with respect to ENSO, which has a considerable influence on the mean location of TC genesis in the WNP. Our results indicate that both east–west contrast of mean genesis location and associated changes in TOF are predictable mainly through better predictions of SST and lower tropospheric large-scale vorticity response. These results indicate that the models can reproduce the major basic mechanisms that link TC genesis with large-scale circulation.

On the multiyear timescale, the skillful prediction of the number of TCs is difficult in the WNP, at least in our hindcast. However, the 1–3-year prediction starting in the year 1998 reasonably captures the observed major characteristics of TC activity associated with the Pacific climate shift during the late 1990s (CH12), and model initialization improves the prediction skill. The strong relationship between the observed TC activity and the oceanic climate shift suggests that the improvement in SST prediction associated with this shift is responsible for better prediction of multiyear TC activity.

Potential NF change in TC activity is also investigated by future ensemble projection. The mean TC number decreases significantly in all models, even in the NF (2016–2035), when global warming is less prominent than that at the end of this century. The projected NF changes in TGF and TOF indicate significant reduction of TC genesis and occurrence frequency, particularly over the western part of the WNP. A possible mechanism for the projected reduction in TC genesis is investigated, considering the changes in large-scale environmental conditions that are assumed to influence TC genesis. Although it is difficult to quantitatively estimate the extent to which environmental factors could decrease the TC genesis number, a comparison of the projected pattern with the TGF indicates that the projected changes in lower tropospheric relative vorticity (ζ_{850}), relative humidity (Rh_{700}), and vertical wind shear (V_{shear}) are

likely responsible for the reduction of TC genesis in the WNP.

The models project a statistically significant warming of the entire tropical and subtropical upper ocean in the NF. However, the increase in SST is nonuniform in that the eastern tropical Pacific exhibits more pronounced warming. This change in SST accompanies the weakening of Walker circulation via redistribution of tropical convection activity, which appears to be responsible for changes in environmental conditions (e.g., ζ_{850}, Rh_{700}, and V_{shear}) in the WNP. Therefore, we conclude that the projected reduction of TC genesis in the WNP is likely due to unfavorable changes in the local environmental fields through the weakening of Walker circulation.

Recently, Villarini and Vecchi (2012) attempted to assess the dominant sources of uncertainty in future projections of TC numbers in the NA by using 17 CMIP5 models. They showed that the NF projection uncertainty arises mainly from internal variability (internal variability uncertainty) and from imperfect knowledge of how the climate system responds to changes in radiative forcing (response uncertainty). Although this assessment targeted the NA, similar features are likely to exist in the WNP. Therefore, uncertainty in internal variability must be reduced to make NF projection more reliable. However, as shown in this study, skillful prediction of TC activity associated with internal variability on multiyear or decadal timescales is likely difficult in the WNP, at least in our hindcast. Therefore, further investigation is required to improve understanding of multiyear or decadal variability in TC activity.

On the other hand, our initialized hindcasts show reasonable predictability of interannual variation in TC activity, particularly that associated with ENSO. This result suggests that our initialization and prediction system could be used for the seasonal prediction of TC activity in the WNP. In the present study, the initial values have been chosen for decadal ensemble prediction; therefore, these initial values are not optimized for seasonal prediction. Thus, it is expected that skillful seasonal prediction of TC activity could be obtained using more appropriate initial values.

Acknowledgements

The authors wish to thank Dr. Murakami and Dr. Yoshimori and two anonymous reviewers for their valuable comments and useful suggestions for the improvement of manuscript. This work is supported by the Japanese Ministry of Education, Culture, Sports, Science, and Technology through the Innovative Program of Climate Change Projection for the 21st Century (the KAKUSHIN Program). The simulations were performed with the Earth Simulator at the Japan Agency for Marine–Earth Science and Technology.

References

Bengtsson, L. I., K. Hodges, M. Esch, N. Keenlyside, L. Kornblueh, J.-J. LUO, and T. Yamagata, 2007: How may tropical cyclones change in a warmer climate? *Tellus A*, **59**, 539–561.

Bister, M., and K. A. Emanuel, 1998: Dissipative heating and hurricane intensity. *Meteorol. Atmos. Phys.*, **65**, 233–240.

Bister, M., and K. A. Emanuel, 2002: Low frequency variability of tropical cyclone potential intensity. 1. interannual to interdecadal variability. *J. Geophys. Res.*, **107**, 4801, doi: 10.1029/2001JD000776.

Bloom, S. C., L. L. Takacs, A. M. da Silva, and D. Ledvina, 1996: Data assimilation using incremental analysis updates. *Mon. Wea. Rev.*, **124**, 1256–1271.

Camargo, S. J., K. A. Emanuel, and A. H. Sobel, 2007: Use of a genesis potential index to diagnose ENSO effects on tropical cyclone genesis. *J. Climate*, **20**, 4819–4834.

Chan, J. C. L., 2007: Interannual variations of intense typhoon activity. *Tellus A*, **59**, 455–460.

Chen, J.-H., and S.-J. Lin, 2011: The remarkable predictability of interannual variability of Atlantic hurricanes during the past decade. *Geophys. Res. Lett.*, **38**, L11804, doi: 10.1029/2011GL047629.

Chia, H. H., and C. F. Ropelewski, 2002: The interannual variability in the genesis location of tropical cyclones in the Northwest Pacific. *J. Climate*, **15**, 2934–2944.

Chikamoto, Y., M. Kimoto, M. Ishii, T. Mochizuki, T. T. Sakamoto, H. Tatebe, Y. Komuro, M. Watanabe, T. Nozawa, H. Shiogama, M. Mori, S. Yasunaka, and Y. Imada, 2013: An overview of decadal climate predictability in a multi-model ensemble by climate model MIROC. *Climate Dyn.*, **40**, 1201–1222.

Chikamoto, Y., M. Kimoto, M. Ishii, M. Watanabe, T. Nozawa, T. Mochizuki, H. Tatebe, T. T. Sakamoto, Y. Komuro, H. Shiogama, M. Mori, S. Yasunaka, Y. Imada, H. Koyama, M. Nozu, and F.-F. Jin, 2012: Predictability of a stepwise shift in Pacific climate during the late 1990s in hindcast experiments using MIROC. *J. Meteor. Soc. Japan*, **90A**, 1–21.

Collins, M., and M. R. Allen, 2002: Assessing the relative roles of initial and boundary conditions in interannual to decadal climate predictability. *J. Climate*, **15**, 3104–3109.

Emanuel, K. A., and D. S. Nolan, 2004: Tropical cyclone activity and the global climate system. In *Preprints*, *26th Conf. on Hurricanes and Tropical Meteorology*, *Miami*, *FL. Amer. Meteor. Soc.*, **10A**, 240–241.

Emanuel, K., R. Sundararajan, and J. Williams, 2008: Hurricanes and global warming: results from downscal-

ing IPCC AR4 simulations. *Bull. Amer. Meteor. Soc.*, **89**, 347–367.

Gray, W. M., 1975: *Tropical cyclone genesis*. Dept. of Atmospheric Science, Colorado State University, **234**, 121 pp.

Gualdi, S., E. Scoccimarro, and A. Navarra, 2008: Changes in tropical cyclone activity due to global warming: Results from a high-resolution coupled general circulation model. *J. Climate*, **21**, 5204–5228.

Hasumi, H., and S. Emori, 2004: K-1 coupled model (MIROC) description. *Center for Climate System Research, University of Tokyo*, K-1 Tech. Rep., **1**, 1–34.

Hawkins, E., and R. Sutton, 2009: The potential to narrow uncertainty in regional climate predictions. *Bull. Amer. Meteor. Soc.*, **90**, 1095–1107.

Hoffman, R. N., and E. Kalnay, 1983: Lagged average forecasting, an alternative to Monte Carlo forecasting. *Tellus A*, **35**, 100–118.

Ishii, M., and M. Kimoto, 2009: Reevaluation of historical ocean heat content variations with time-varying XBT and MBT depth bias corrections. *J. Oceanogr.*, **65**, 287–299.

Ishii, M., M. Kimoto, K. Sakamoto, and S. Iwasaki, 2006: Steric sea level changes estimated from historical ocean subsurface temperature and salinity analyses. *J. Oceanogr.*, **62**, 155–170.

Keenlyside, N. S., M. Latif, J. Jungclaus, L. Kornblueh, and E. Roeckner, 2008: Advancing decadal-scale climate prediction in the North Atlantic sector. *Nature*, **453**, 84–88.

Kirtman, B. P., J. Shukla, M. Balmaseda, N. Graham, C. Penland, Y. Xue, and S. Zebiak, 2001: Current status of ENSO forecast skill: A report to the CLIVAR working group on seasonal to interannual prediction. WCRP Informal Report No 23/01, ICPO Publication, No. 56, 26 pp.

Knutson, T. R., J. L. McBride, J. Chan, K. Emanuel, G. Holland, C. Landsea, I. Held, J. P. Kossin, A. K. Srivastava, and M. Sugi, 2010: Tropical cyclones and climate change. *Nature Geosci.*, **3**, 157–163.

Li, T., M. Kwon, M. Zhao, J. Kug, J. Luo, and W. Yu, 2010: Global warming shifts Pacific tropical cyclone location. *Geophys. Res. Lett*, **37**, L21804, doi: 10.1029/2010GL045124.

McDonald, R. E., D. G. Bleaken, D. R. Cresswell, V. D. Pope, and C. A. Senior, 2005: Tropical storms: representation and diagnosis in climate models and the impacts of climate change. *Climate Dyn.*, **25**, 19–36.

Meehl, G. A., L. Goddard, J. Murphy, R. J. Stouffer, G. Boer, G. Danabasoglu, K. Dixon, M. A. Giorgetta, A. M. Greene, E. Hawkins, and others, 2009: Decadal prediction. *Bull. Amer. Meteor. Soc.*, **90**, 1467–1485.

Mochizuki, T., Y. Chikamoto, M. Kimoto, M. Ishii, H. Tatebe, Y. Komuro, T. T. Sakamoto, M. Watanabe, and M. Mori, 2012: Decadal prediction using a recent series of MIROC global climate models. *J. Meteor. Soc. Japan*, **90A**, 373–383.

Mochizuki, T., M. Ishii, M. Kimoto, Y. Chikamoto, M. Watanabe, T. Nozawa, T. T. Sakamoto, H. Shiogama, T. Awaji, N. Sugiura, T. Toyoda, S. Yasunaka, H. Tatebe, and M. Mori, 2010: Pacific decadal oscillation hindcasts relevant to near-term climate prediction. *PNAS*, **107**, 1833–1837.

Moss, R., M. Babiker, S. Brinkman, E. Calvo, T. Carter, J. Edmonds, I. Elgizouli, S. Emori, E. Lin, K. Hibbard, and others, 2008: *Towards new scenarios for analysis of emissions, climate change, impacts, and response strategies*. Pacific Northwest National Laboratory (PNNL), Richland, WA, USA.

Moss, R., J. Edmonds, K. Hibbard, M. Manning, S. Rose, D. van Vuuren, T. Carter, S. Emori, M. Kainuma, T. Kram, and others, 2010: The next generation of scenarios for climate change research and assessment. *Nature*, **463**, 747–756.

Murakami, H., B. Wang, and A. Kitoh, 2011: Future change of Western North Pacific typhoons: Projections by a 20-km-mesh global atmospheric model. *J. Climate*, **24**, 1154–1169.

Murakami, H., Y. Wang, H. Yoshimura, R. Mizuta, M. Sugi, E. Shindo, Y. Adachi, S. Yukimoto, M. Hosaka, S. Kusunoki, and others, 2012: Future changes in tropical cyclone activity projected by the new high-resolution MRI-AGCM. *J. Climate*, **25**, 3237–3260.

Nakicenovic, N., J. Alcamo, G. Davis, B. De Vries, J. Fenhann, and others, 2000: *Special Report on Emissions Scenarios* (*SRES*). *Working Group III of the Intergovernmental Panel on Climate Change* (*IPCC*). IPCC (ed.), Cambridge University Press, Cambridge, UK.

Nozawa, T., T. Nagashima, H. Shiogama, and S. A. Crooks, 2005: Detecting natural influence on surface air temperature change in the early twentieth century. *Geophys. Res. Lett.*, **32**, L20719, doi: 10.1029/2005GL023540.

Onogi, K., J. Tsutsui, H. Koide, M. Sakamoto, S. Kobayashi, H. Hatsushika, T. Matsumoto, N. Yamazaki, H. Kamahori, K. Takahashi, and others, 2007: The JRA-25 reanalysis. *J. Meteor. Soc. Japan*, **85**, 369–432.

Oouchi, K., J. Yoshimura, H. Yoshimura, R. Mizuta, S. Kusunoki, and A. Noda, 2006: Tropical cyclone climatology in a global-warming climate as simulated in a 20 km-mesh global atmospheric model: Frequency and wind intensity analyses. *J. Meteor. Soc. Japan*, **84**, 259–276.

Pohlmann, H., J. Jungclaus, A. Köhl, D. Stammer, and J. Marotzke, 2009: Initializing decadal climate predictions with the GECCO oceanic synthesis: Effects on the North Atlantic. *J. Climate*, **22**, 3926–3938.

Sakamoto, T. T., Y. Komuro, T. Nishimura, M. Ishii, H. Tatebe, H. Shiogama, A. Hasegawa, T. Toyoda, M. Mori, T. Suzuki, Y. Imada, T. Nozawa, K. Takata, T. Mochizuki, K. Ogochi, S. Emori, H. Hasumi, and M. Kimoto, 2012: MIROC4h: A new high-resolution

atmosphere-ocean coupled general circulation model. *J. Meteor. Soc. Japan*, **90**, 325–359.

Smith, D. M., S. Cusack, A. W. Colman, C. K. Folland, G. R. Harris, and J. M. Murphy, 2007: Improved surface temperature prediction for the coming decade from a global climate model. *Science*, **317**, 796–799.

Smith, D. M., R. Eade, N. J. Dunstone, D. Fereday, J. M. Murphy, H. Pohlmann, and A. A. Scaife, 2010: Skilful multi-year predictions of Atlantic hurricane frequency. *Nature Geosci*., **3**, 846–849.

Stowasser, M., Y. Wang, and K. Hamilton, 2007: Tropical cyclone changes in the Western North Pacific in a global warming scenario. *J. Climate*, **20**, 2378–2396.

Sugi, M., H. Murakami, and J. Yoshimura, 2009: A reduction in global tropical cyclone frequency due to global warming. *SOLA*, **5**, 164−167.

Sugi, M., A. Noda, and N. Sato, 2002: Influence of the global warming on tropical cyclone climatology: An experiment with the JMA global model. *J. Meteor. Soc. Japan*, **80**, 249–272.

Tatebe, H., M. Ishii, T. Mochizuki, Y. Chikamoto, T. Sakamoto, Y. Komuro, M. Mori, S. Yasunaka, M. Watanabe, K. Ogochi, T. Suzuki, T. Nishimura, and M. Kimoto, 2012: The initialization of the MIROC climate models with hydrographic data assimilation for decadal prediction. *J. Meteor. Soc. Japan*, **90A**, 275–294.

Taylor, K. E., 2001: Summarizing multiple aspects of model performance in a single diagram. *J. Geophys. Res*, **106**, 7183–7192.

Taylor, K. E., R. J. Stouffer, and G. A. Meehl, 2012: An overview of CMIP5 and the experiment design. *Bull. Amer. Meteor. Soc*., **93**, 485–498.

Tokinaga, H., S. Xie, A. Timmermann, S. McGregor, T. Ogata, H. Kubota, and Y. M. Okumura, 2012: Regional patterns of tropical Indo-Pacific climate change: Evidence of the Walker circulation weakening. *J. Climate*, **25**, 1689–1710.

Tu, J., C. Chou, and P. Chu, 2009: The abrupt shift of typhoon activity in the vicinity of Taiwan and its association with Western North Pacific-east Asian climate change. *J. Climate*, **22**, 3617–3628.

Vecchi, G. A., and B. J. Soden, 2007: Global warming and the weakening of the tropical circulation. *J. Climate*, **20**, 4316–4340.

Villarini, G., and G. A. Vecchi, 2012: Twenty-first-century projections of North Atlantic tropical storms from CMIP5 models. *Nature Climate Change*, **2**, 604–607.

Wang, B., and J. C. L. Chan, 2002: How strong ENSO events affect tropical storm activity over the Western North Pacific. *J. Climate*, **15**, 1643–1658.

Watanabe, M., T. Suzuki, R. O'ishi, Y. Komuro, S. Watanabe, S. Emori, T. Takemura, M. Chikira, T. Ogura, M. Sekiguchi, K. Takata, D. Yamazaki, T. Yokohata, T. Nozawa, H. Hasumi, H. Tatebe, and M. Kimoto, 2010: Improved climate simulation by MIROC5: Mean states, variability, and climate sensitivity. *J. Climate*, **23**, 6312–6335.

Yokoi, S., and Y. N. Takayabu, 2009: Multi-model projection of global warming impact on tropical cyclone genesis frequency over the Western North Pacific. *J. Meteor. Soc. Japan*, **87**, 525–538.

Zhao, M., I. M. Held, S.-J. Lin, and G. A. Vecchi, 2009: Simulations of global hurricane climatology, interannual variability, and response to global warming using a 50-km resolution GCM. *J. Climate*, **22**, 6653–6678.